RSC Advances

PAPER

View Article Online
View Journal | View Issue

Cite this: *RSC Adv.*, 2021, **11**, 8314

Insight into single-element nobel metal anisotropic silver nanoparticle shape-dependent selective ROS generation and quantification†

Jabran Ahmad,*[a] Abdul Ghaffar Memon,*[ab] Asif Ahmed Shaikh,[b] Tariq Ismail,[c] Abdulmoseen S. Giwa[d] and Awais Mahmood[e]

The biocidal action mechanism of single element noble metal anisotropic nanoparticles has remained a perplexing challenge. Herein, we investigated the photogenerated anisotropic AgNP ROS production kinetics and each ROS species' direct impact on Gram-negative and Gram-positive bacteria. Three shapes (Triangular, Cubes, Rods) of AgNP with excellent morphology were fabricated *via* plasmon mediated synthesis. The results demonstrated a distinct bactericidal capacity of each NP shape where Ag-Tri outperformed Ag-Cub and Ag-Rod by displaying complete bacterial mutilation at a very low dose of 18 μg mL^{-1} for the shortest exposure time of 180 min. In contrast, Ag-Cub needed 66.6% higher NP concentration, while Ag-Rod was unable to achieve complete bacterial mutilation. In contrast to $O_2^{\bullet-}$, (Ag-Tri 69 ± 3.2, Ag-Cub 72 ± 2.9, Ag-Rod 68.5 ± 3.7 μM), the amount of $^{\bullet}OH$ production was considerably lower (Ag-Tri 11 ± 1.6, Ag-Cub 10.4 ± 1.9, Ag-Rod 11.3 ± 2.2 μM), while $^1O_2$ remained undetected for all NP shapes. Moreover, antimicrobial activity of selective ROS species revealed $O_2^{\bullet-}$ as a dominant species among ROS. However, $O_2^{\bullet-}$ was not found as a decisive factor in microbial mutilation. SEM images affirmed the significance of the specific geometrical shape and its resultant attachment to bacterial surface to be of paramount significance. The sharp-tip morphology with high-atom density active {111} facets played a pivotal role in physically deteriorating bacterial cells. Ag-Tri morphology in synchronization with ROS species assisted its wedging into the bacterial cell, translating into superior and multifaceted antibacterial performance.

Received 17th December 2020
Accepted 6th February 2021

DOI: 10.1039/d0ra10616j

rsc.li/rsc-advances

1. Introduction

Anisotropic nanostructures have recently made their mark in the realm of nanoparticles as ultra-reactive materials. Their unique morphology besets broad spectra of physicochemical properties that are far superior to their isotopic counterparts. Anisotropic silver nanoparticles (AgNP) have shown great promise as robust shape-dependent microbial mutilator with their multifaceted morphology and high surface by volume ratio. However, limited data is available in this regard in which different shapes were tested and compared for biocidal properties.

Gao *et al.*, reported higher biocidal capabilities of silver nano-spheres when compared with triangular silver nano-particles.[1] In one study, the higher antimicrobial effect of silver nano-cubes over silver nano-spheres and nano-wires against *E. coli* is investigated.[2] However, other studies showed superior performance of silver triangular nanoparticles when tested with nano-spheres and nano-rods.[3,4] These variations in results may arise from the differences in synthesis route employed to obtain different shapes of anisotropic nanoparticles in the same studies, as the synthesis method and the surface coating dictates the final efficacy of the nanoparticle.[5–8]

Moreover, there are deviant views about the facet reactivity and their resultant effect on the antibacterial property. Several reports advocated the presence of {111} facets to be responsible for higher biocidal effect,[9] while other attributed {100} facets to be more reactive due to their higher surface energies.[10–12]

The production of ROS and its resultant deleterious effect on microbes is well reported. The ROS usually contain hydroxyl radicals ($^{\bullet}OH$), superoxide ions ($O_2^{\bullet-}$), hydrogen peroxide (H_2O_2), and singlet oxygen ($^1O_2$).[13] However, very little is known about the direct impact of each ROS species on particular bacteria. Furthermore, to the best of the author's knowledge, there are no studies yet conducted that incorporate the plasmon

[a]*State Key Joint Laboratory of ESPC, School of Environment, Tsinghua University, Beijing 100084, China. E-mail: jibranahmad888@hotmail.com; Tel: +33610117616*

[b]*Department of Environmental Engineering, NED University of Engineering and Technology, Karachi 75270, Pakistan. E-mail: abdulghaffar@neduet.edu.pk; Fax: +92 3332348022; Tel: +92 2199261261-8 (Ext: 2225/2346)*

[c]*Department of Plant Protection and Production, Szent Istvan University, Hungary*

[d]*Green Intelligence Environmental School, Yangtze Normal University, Chongqing 408100, China*

[e]*Computation-based Science and Technology Research Center (CaSToRC), The Cyprus Institute, Nicosia, Cyprus*

† Electronic supplementary information (ESI) available. See DOI: 10.1039/d0ra10616j

mediated synthesis method to produce different anisotropic AgNPs using the same silver seed in one study to test their efficacy against microbes. Moreover, there is no research available on the ROS generation of single element noble metal nanoparticles based on their different shapes and no data available on selective ROS species' biocidal effect on microbes.

This research focuses on investigating the unmodified single element noble metal anisotropic AgNP shape-dependent ROS quantification. Moreover, we have also investigated the selective ROS species action on Gram-positive and Gram-negative bacteria. Three different shapes of AgNP, triangular, cubes and rods, were successfully fabricated solely by plasmon mediated synthesis, by using the same silver seed. Thus, we have effectively removed the fabrication perplexity and bias among the tested AgNP shapes. This study provides fundamental information regarding AgNPs morphology dependent bacterial inhibition performance. Moreover, it could be useful for developing efficient AgNPs structures with unique geometrical features for enhanced antimicrobial performance.

2. Materials and methods

Materials

The XXT (2,3-bis (2-methoxy-4-nitro-5-sulfophehyl)-2*H*-tetrazolium-5-carboxanilide), *p*chlorobenzoic acid (*p*CBA) furfuryl alcohol (FFA), superoxide dismutase (SOD) isopropanol, glycerol, silver nitrate ($AgNO_3$), trisodium citrate, sodium hydroxide (NaOH), and bis(*p*-sulfonatophenyl)-phenylphosphine dihydrate dipotassium salt (BSPP) were purchased from Aldrich. All reagents were used as received, and water from the Millipore Milli-Q Purification system was used in the entire experiment. Refer to ESI for the chemicals, instruments, and other equipment utilized in this study (Page S-2†).

Nanoparticles fabrication

Anisotropic AgNPs were fabricated by Plasmon mediated synthesis. Three different shapes were fabricated, triangular, cubes and rods and were represented Ag-Tri, Ag-Cub and Ag-Rod. As-prepared anisotropic AgNPs were extensively characterized by various characterization tools to evaluate their shape, size, crystal structure and mono-dispersity. The detailed account of the fabrication route and elaborative analysis of NP characterization is described in the ESI (S. Note 1, Fig S1, S2, S3, Table S1†).

Photochemical experiments

For assessing antibacterial activity, ROS production, and the measurement of Ag ion release, samples were irradiated with UV-lamp with a wavelength of 254 nm for 15 min. The NP suspension was prepared with the concentration of 5 mg L^{-1}. In each experiment, 100 mL of the suspension was poured into a quartz beaker and was subjected to UV irradiation while keeping the reaction mixture temperature constant at 24 °C by a constant temperature water bath. During the experiment, water volume was carefully monitored to examine the possible water loss from evaporation. Ag ion quantification was performed by inductively coupled plasma mass spectroscopy (ICP-MS). The 5 mL of NP suspension at a concentration of 5 mg L^{-1}, after UV irradiation, were collected and digested with acid. Ag ion release in the dark was also performed to detect the Ag ion release without UV exposure. The background ion concentration was subtracted from the concentration of released ions under UV irradiation.

Antimicrobial testing

To study the bacteriostatic effect of the as-prepared NPs, minimal inhibitory concentration (MIC) *via* broth dilution was performed. Meanwhile, bactericidal properties were evaluated through a minimal bactericidal concentration (MBC) test using the standard plate count method against *E. coli* and *S. aureus*. These microbes were isolated from the wastewater stream in an unrelated work and were identified by 16S rRNA sequence analysis. In all the antibacterial assessment experiments, the anisotropic AgNPs were first irradiated with a UV lamp (wavelength 254 nm) for 15 min in a separate quartz tube before mixing it with bacterial suspension. The silver ion release (with and without UV irradiation), the ROS production under dark conditions and their resultant effects on bacteria were subtracted from the bactericidal effect and ROS production under UV irradiation.

MIC and MBC evaluation

Luria Bertani (LB) nutrient medium was used for all bacterial cultures. The cultures were revived using LB broth and sub-cultured after regular intervals. The MIC is defined as the lowest concentration of the antimicrobial agent that inhibits the microorganism's growth. In this study, the MIC is determined by batch culture containing different concentrations of anisotropic AgNPs in suspension. All the apparatus and glassware were sterilized at 121 °C for 20 min before being utilized. After culturing and harvesting, all the strains were re-suspended at the final concentration to maintain the initial concentration of 10^7 colony forming unit per milliliter (CFU mL^{-1}) by adjusting the optical density 0.15 at a wavelength of 600 nm *via* spectrophotometry as per McFarland scale. The MIC estimation procedure was followed by UV irradiation of anisotropic AgNPs dispersed in phosphate buffer solution (PBS) for 15 min under the pH of 7.2. The bacterial cells (0.1 μL) were inoculated into a fresh medium of 1 mL and were supplemented with various concentrations of NPs and then set for incubation in an orbital shaker at 110 rpm under 37 °C for 24 h. Bacterial growth was observed by OD measurements having different concentrations of NPs. To evaluate the MBC, which is defined as the lowest concentration of NP required to kill bacteria completely, 100 μL solution was taken from the tubes without visible bacterial growth and plated on the agar plate. The tubes containing only the bacterial suspension without NPs were taken as control. The plates were incubated at 37 °C for 24 h. The grown colonies were counted, and the results were plotted in terms of loss viability percentage by eqn (1):

$$\text{Loss viability percent } (\%) = n/N \times 100 \quad (1)$$

where n is the number of bacterial cells (CFU) in the NPs laden suspensions and N is the CFU value of the control. The CFU values were converted into log values for data representation as log reduction. All experiments were performed in triplicates.

Killing rate of anisotropic AgNPs against *E. coli* and *S. Aureus*

The shape-dependent killing rate for *E. coli* and *S. aureus*, inoculated with PBS solution at a bacterial concentration of 10^7–10^8 CFU mL^{-1} containing different UV irradiated concentrations Ag-Tri and Ag-Cub and Ag-Rod was determined. Bacterial cells were grown in LB medium and were harvested by centrifugation at 12 000 rpm and suspended in sterilized 1.0 M, PBS solution followed by serial dilution. The initial concentration was adjusted by absorbance measurements at 600 nm as per McFarland standards. The suspensions were supplemented with different concentrations of Ag-Tri, Ag-Cub, Ag-Rod and incubated at 37 °C. The bacterial samples were collected at different intervals between 0–300 min of incubation, serially diluted, and plated on agar plates at 37 °C for 24 h. The viable cells were enumerated in terms of CFU, and the results were plotted as a percent decrease in the cell population. Suspensions without Ag were run in parallel as a control. All experiments were performed in triplicates, and standard errors of the means were calculated.

ROS species detection

XXT (2,3-bis(2-methoxy-4-nitro-5-sulfophehyl)-2*H*-tetrazolium-5-carboxanilide), 100 μM, 20 μM *p*-chlorobenzoic acid (*p*CBA) and 0.85 mM furfuryl alcohol (FFA) were used as indicators for $O_2^{\bullet -}$, $^{\bullet}OH$ and $^1O_2$ respectively, and their ROS scavengers, superoxide dismutase (SOD) isopropanol and glycerol were purchased from Sigma-Aldrich. For the determination of $O_2^{\bullet -}$, 100 mL NP suspension loaded with XXT was exposed to UV irradiation for different time periods for up to 30 h. The 1 mL of suspension was taken and poured into the quartz vial. The concentration of XXT-formazan was measured by UV-Vis spectrophotometer UV-3101PC (Shimadzu, Japan), which is the resultant product from the reduction of XXT by $O_2^{\bullet -}$. For $^{\bullet}OH$ and $^1O_2$, after UV exposure, 3 mL of the suspension was collected and filtered by Amicon filter, the pore size of 1–2 nm (Amicon Ultracel 3K, Millipore USA). The filtrate was analyzed with high-performance liquid chromatography for the concentration of *p*CBA and FFA. All three types of ROS stoichiometrically react with their relevant indicator in a mole ratio of 1 : 1.

For the determination of background ROS production without UV irradiation, the experiments were also performed in the dark. The molar concentration of each ROS species was computed by the following eqn (2).

$$C = \frac{\int_0^T (C_0 - C_t)\mathrm{d}t}{T} \quad (2)$$

Where C is the average molar concentration (μM) of each type of ROS, C_0 is the initial molar concentration of indicator (μM), C_t is the molar concentration of the indicator (μM) after a UV irradiation time of t (h) and T is the UV exposure time of 30 h.

3. Result and discussion

Morphology and crystal structure of anisotropic AgNP

Triangular (Ag-Tri), cube (Ag-Cub) and rods (Ag-Rod) were successfully fabricated by using the same silver seed at room temperature. SPR dictates the optical absorption spectra of metal NP, which shifts to a longer wavelength with increased particle size. Multiple peaks were observed for Ag-Tri, Ag-Cub, and Ag-Rod, prepared by plasmon-mediated synthesis as anisotropic NP give rise to more than one absorption peak due to their asymmetrical orientation. Fig. 1(a) shows the peaks for Ag-Tri at ~520 nm, and ~690 nm, while the peaks at ~420 nm and ~565 nm shows the characteristics of the typical Ag-Cub, which correspond to the out-of-plane quadrupole, the in-plane quadrupole, and the in-plane dipole plasmon resonance modes of the Ag-Tri and Ag-Cub. Metallic Ag-Tri and Ag-Rod, crystallized in the face-centered cubic (fcc) structure with basal {111} lattice planes, while Ag-Cub was mainly dominated by {100} facet (Fig. 1(b)).

All NP displayed monodispersity, while Ag-Tri were found to be arranged in a tip-to-tip manner on the silicon wafer, forming so-called "hot spots." Fig. 2 showed the SEM images of the three different shapes of anisotropic AgNP with a size ranging from 26 to 138 nm. Fabricated NP displayed excellent morphology and high crystallinity.

Antibacterial assessment of anisotropic nanoparticles

All samples of anisotropic AgNP were first irradiated with UV-lamp with a wavelength of 254 nm for 15 min. The irradiated NPs were further subjected to sequential assessment as depicted in Fig. 3.

The minimal inhibitory concentration (MIC) was established for all anisotropic AgNP of size ranging from 30 nm to 100 nm. Fig. 4 demonstrated the shape and dose-dependent growth profile of *E. coli* and *S. aureus* with various anisotropic Ag-Tri, Ag-Cub, and Ag-Rod concentrations. The results revealed that bacterial growth was affected by all anisotropic AgNP compared

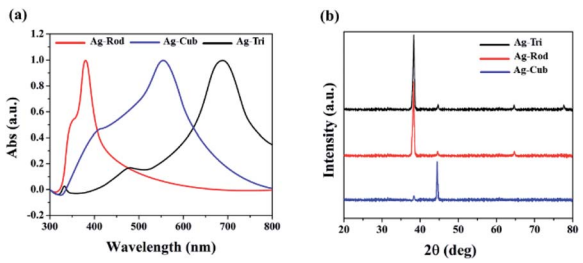

Fig. 1 (a) Illustrated the UV spectra of anisotropic AgNP with their characteristic peaks at ~360 and 380 nm for Ag-Rod 420 and ~565 nm for Ag-Cub and the peaks at ~520 nm and ~690 nm for Ag-Tri. (b) XRD spectra of anisotropic AgNP of Ag-Tri, Ag-Rod and Ag-Cub respectively.

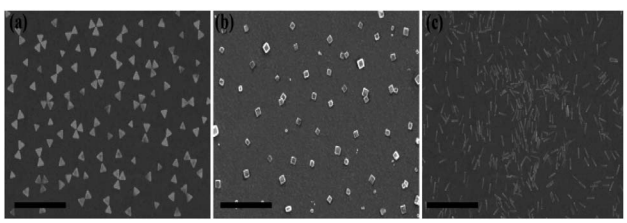

Fig. 2 SEM images of anisotropic AgNP at excitation wavelength of 600 nm, 450 nm and 700 nm of (a) Ag-Tri, (b) Ag-Cub and (c) Ag-Rod respectively. Scale bar 400 nm.

to the bacterial culture grown in the absence of nanoparticles (control). The Ag-Tri displayed noticeable retardation in bacterial growth at a concentration of 4 μg mL^{-1} for *E. coli* with a 72% reduction in cell density. The bacterial growth was observed to be retarded with a 44% reduction in cell density at a concentration of 14 μg mL^{-1} against *S. aureus*. The complete inhibition of growth was achieved at a concentration of 12 μg mL^{-1} and 22 μg mL^{-1} for *E. coli* and *S. aureus,* respectively.

The MIC values for Ag-Cub were 20 μg mL^{-1} and 36 μg mL^{-1} for *E. coli* and *S. aureus,* respectively, 66.6% and 63.6% higher than that of Ag-Tri concentrations. Ag-Rod exhibited the highest MIC values among all NP used. The detectable growth inhibition of *E. coli* by Ag-Rod was noticed at a concentration of 35 μg mL^{-1}, which are 8.7 and 3.5 folds higher than that of Ag-Tri concentration. The complete inhibition was achieved at 65 μg mL^{-1}. For *S. aureus*, the required concentration to establish MIC was 10^5 μg mL^{-1} for Ag-Rod, which is 4.7 folds higher concentration than Ag-Tri, and 2.9 folds higher than that of Ag-Cub. It is noteworthy that MIC values demonstrated by these anisotropic NP were significantly lower than MIC values reported by commercially manufactured AgNPs at a bacterial concentration of 10^5 CFU mL^{-1}.[14] The MIC values demonstrated by all anisotropic AgNPs in this research were in the range of 12 μg mL^{-1} to 105 μg mL^{-1}, which is significantly lower as was reported in other studies that incorporated different shapes for antibacterial purpose. Acharya and co-workers reported silver nano-rods MIC values of 340 μg mL^{-1} for *E. coli*, which is nearly three times higher concentration compared to this work.[15]

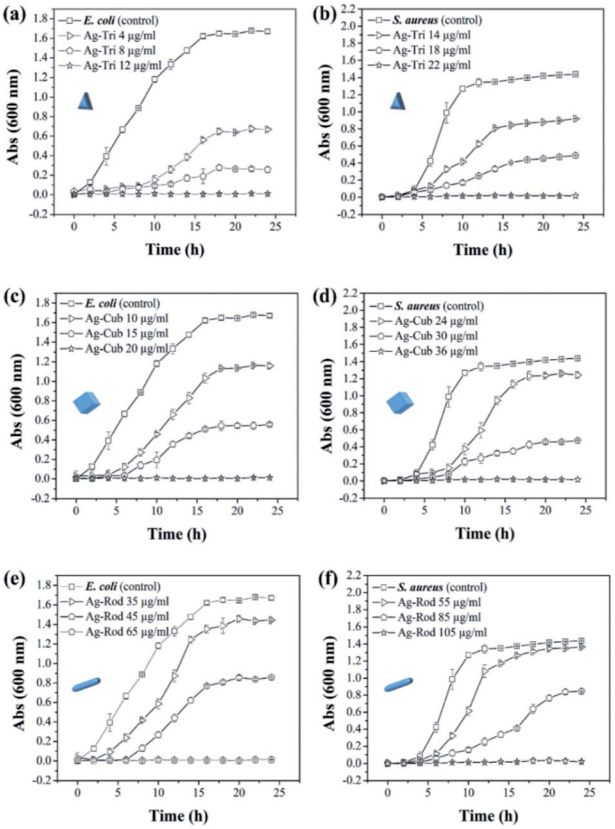

Fig. 4 Growth profile of *E. coli* and *S. aureus* for the determination of MIC values of anisotropic AgNP in 24 h (a) Ag-Tri *E. coli* (b) Ag-Tri *S. aureus* (c) Ag-Cub *E. coli* (d) Ag-Cub *S. aureus* (e) Ag-Rod *E. coli* (f) Ag-Rod *S. aureus*.

Killing rate of anisotropic AgNPs against *E. coli* and *S. Aureus*

Growth inhibition in microbes does not guarantee complete bacterial destruction. Bacteria can be inactivated at certain NP concentrations, but it has the tendency to recover and proliferate. For the complete bacterial mortality, the killing rate of NP against both bacterial strains were performed. Minimal bactericidal concentrations (MBC) were set based on previously tested MIC values of all NP. To the best of our knowledge, this is the first study that has systematically illustrated in great detail the MIC/MBC values of different shapes of anisotropic AgNPs against Gram-negative and G-positive bacteria. The killing rate of both bacterial strains was studied for all three shapes of anisotropic AgNPs. The MBC values were found to be in the range of 12 to 18, 20 to 30 and 65 to 90 μg mL^{-1} against *E. coli* for Ag-Tri. Ag-Cub and Ag-Rod. The required MBC of nanoparticles against *S. aureus* was found to be comparatively higher than that of Gram-negative bacteria. Against *S. aureus*, the nanoparticle concentration was found to be in the range of 22 to 30, 35 to 45, and 105 to 170 μg mL^{-1} for Ag-Tri, Ag-Cub and Ag-Rod, respectively. Ag-Tri exhibited the highest rate of killing against both bacterial strains.

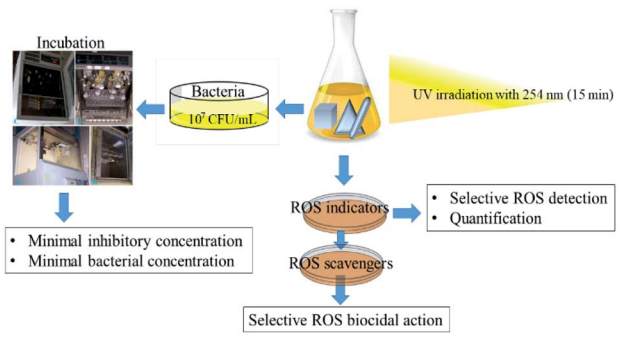

Fig. 3 Schematic diagram of the methodological workflow illustrating anisotropic AgNP individual shape UV irradiation to MIC, MBC, and ROS generation and quantification steps.

Fig. 5 illustrates the killing rate of all anisotropic NP against both bacterial strains. Within the first 120 min, 70% of bacterial killing was achieved by Ag-Tri at a concentration of 18 μg mL^{-1}. Ag-Tri achieved 100% bacterial killing at a concentration of 18 μg mL^{-1} against *E. coli* within 180 min of NP exposure. Ag-cub also showed better killing performance against *E. coli*. Ag-Cub took a comparatively longer time duration of 240 min and 66.6% higher NP concentration (30 μg mL^{-1}) than that of Ag-Tri to achieve a 100% bactericidal effect. Ag-Rod displayed inferior bactericidal performance. After 300 min of Ag-Rod exposure to *E. coli* with their MIC concentration (65 μg mL^{-1}), it was only able to reduce the bacterial population by 8%. Ag-Rod showed 87% reduction in *E. coli* population at a 90 μg mL^{-1} concentration, which was three times higher NP concentration than

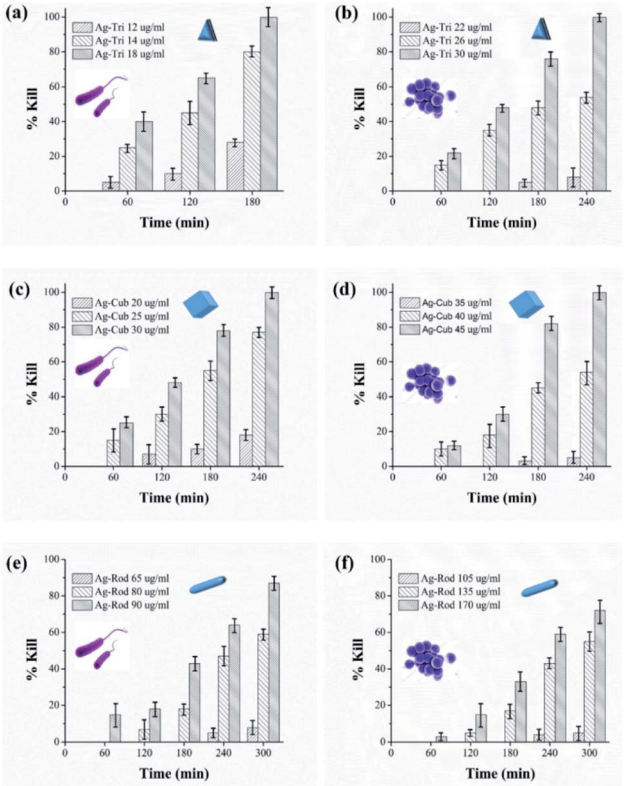

Fig. 5 Killing kinetics of Ag-Tri, Ag-Cub and Ag-Rod against *E. coli* and *S. aureus* over the time duration of zero to 300 min. For visual clarity, the bacterial type is indicated with its shape as inset (*E. coli* with rod shape and *S. aureus* with spherical shape) nanoparticle shape (triangular, cubes and rods) is illustrated with its respective graphic shape in each figure.

Ag-Cub. It was noteworthy that Ag-Tri not only achieved a 100% killing rate by utilizing a minimal dose of NP, but Ag-Tri took the shortest time duration (180 min) to achieve this effect in comparison to other shapes used in this work. All anisotropic NP used in this work showed comparatively higher concentration required against S aureus than that of concentration required to reduce *E. coli* population.

Ag-Rod continued to display inferior performance and was unable to effectively reduce the *S. aureus* population. Only 72% of cell reduction was achieved at a concentration of 170 μg mL^{-1} after 300 min. The established MBC value for Ag-Rod was found to be 310 μg mL^{-1}. A few researchers have also reported high concentrations required by Ag-Rod for antibacterial activity. Acharya and group reported the required concentration of Ag-Rod against *K. pneumonia*, at a bacterial concentration of 10^7 CFU. They reported 720 μg mL^{-1} of Ag-Rod inhibited only 42.635 of *K. pneumonia*.[15]

Ag-Cub achieved above 80% cell reduction in 180 min and 100% bactericidal effect in 240 min at a 45 μg mL^{-1} concentration. Ag-Tri utilized the minimum nanoparticle concentration of just 30 μg mL^{-1} to achieve 100% bactericidal effects against *S. aureus* in 240 min. However, unlike the least time taken by Ag-Tri for complete *E. coli* killing, in the case of *S. aureus*, both Ag-Tri and Ag-Cub took the same time of 240 min to achieve 100% bactericidal effect. The higher resistance of *S. aureus* compared to *E. coli* toward NP might be due to the difference in their cell wall composition. The cell wall of both Gram-negative and Gram-positive bacteria is negatively charged, but the difference in their composition might be a decisive factor in determining susceptibility toward NP. The thickness of the peptidoglycan layer in Gram-positive bacteria, such as *S. aureus*, is around 80 nm, which is just ~8 nm thick in *E. coli*. This arrangement may facilitate the ease in NP biocidal action by Ag ions or by direct cell penetration. Furthermore, studies carried by electrophoretic mobility and by mathematical calculations demonstrated that *E. coli* is more negatively charged and rigid than that of *S. aureus*.[16] The high negative surface can facilitate higher NP binding, resulting in higher toxicity in the NP concentrated regions of bacteria. Several other studies demonstrated higher resistance of Gram-positive bacteria against NP.[17–19]

The results showed the shape, dependent bacterial effect of anisotropic nanoparticles. The antibacterial activity was more prominent in Gram-negative bacteria as compared to Gram-positive bacteria. All anisotropic NP displayed antibacterial effect. Ag-Tri exhibited superior performance among all tested AgNPs shapes, followed by Ag-Cub and Ag-Rod, respectively. Concerning Ag-Tri, Ag-Cub required 1.6 fold Ag-Rod needed 3 fold higher concentrations in comparison to Ag-Cub against *E. coli*. All NP respective MIC and MBC values are summarized in Table 1.

It is interesting to note that low energy {111} facets mainly dominated both Ag-Tri and Ag-Rod. However, unlike Ag-Tri, one-dimensional Ag-Rod had no such sharp edges and vertex. The corners of the rods mainly remained rounded. The low specific surface area of rods can also be the reason behind the reduced activity of Ag-Rod. Furthermore, many rods were found to be in poor contact with the bacterial cell where only the rounded tip of the rod was in contact with the bacterial surface and not the whole particle, due to occupancy by other particles in the area, its natural orientation toward bacteria provided limited contact over several locations.

Fig. 6 provided an in-depth picture of anisotropic AgNPs interaction with bacterial cells. TEM images demonstrated the direct proof of bacterial cell disintegration. It can be seen that the Ag-Tri severely damaged the bacterial wall. The nanoparticles' sharp tips were able to pierce through the bacterial membrane and caused bacterial mutilation at several points in *E. coli* cells. The leakage of intracellular matrix upon Ag-Tri contact can also be visualized clearly, which led to bacterial mortality. Somewhat similar damage was noticed for Ag-Cub. In

Table 1 Established MIC and MBC values of anisotropic AgNP

	MIC μg mL^{-1}		MBC μg mL^{-1}	
NP shape	*E. coli*	*S. aureus*	*E. coli*	*S. aureus*
Ag-Tri	12	22	18	30
Ag-Cub	20	36	30	45
Ag-Rod	65	105	90	170

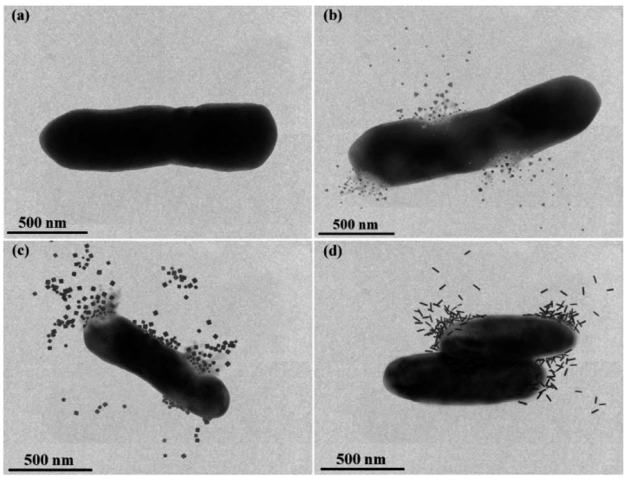

Fig. 6 TEM images showing anisotropic silver nanoparticles interaction with *E. coli*. (a) Healthy *E. coli* cell without nanoparticles exposure (b) Ag-Tri with *E. coli* showed the bacterial mutilation upon contact and resultant membrane disintegration (c) Ag-Cub with *E. coli* showed membrane leakage and compromised of cell integrity (d) Ag-Rod achieved bacterial inactivation and displayed no cellular destruction or cell leakage.

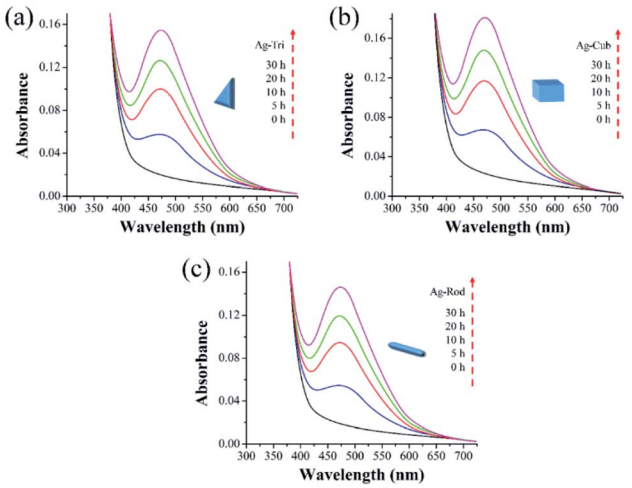

Fig. 7 Superoxide ($O_2^{\bullet-}$) generation kinetics of anisotropic silver nanoparticles under UV irradiation. The spectra generated at 470 nm indicated by the reduction of 100 μM XTT (a) $O_2^{\bullet-}$ generation by Ag-Tri (b) $O_2^{\bullet-}$ by Ag-Cub (c) $O_2^{\bullet-}$ generation by Ag-Rod.

this work, both Ag-Tri and Ag-Cub possess sharp tip morphology. These sharp vertexes played an essential role in bacterial membrane disintegration.

On the contrary, Ag-Rod was found to cause no such damage. Fig. 6(d) showed rods' accumulation on the bacterial surface at multiple sites; although the bacterial cells were inactivated, no visible cell damage in membrane disintegration of cellular leakage was noticed. TEM results for Ag-Rod also explain the possible reason behind lower antibacterial performance compared to its counterparts. Ag-Rod was unable to achieve a 100% bactericidal effect against *E. coli* and *S. aureus*.

Dynamic detection of photo-generated ROS species

This study used three unmodified anisotropic AgNPs to assess three ROS species generation kinetics in an aqueous suspension under UV irradiation at a wavelength of 254 nm. ROS generation's quantitative evaluation was performed under the same experimental conditions, such as light irradiation wavelength, irradiation time, and doze of nanoparticles. The overarching goal was to provide the ROS generation kinetics, ROS quantification and to assess any possible difference of ROS generation between the different shapes of a single-element metallic AgNPs. Fig. 7 shows the changes in the absorption spectrum of anisotropic silver nanoparticles suspension in the presence of XXT during 30 h of experimental duration. The formation of XXT-formazan upon reacting with $O_2^{\bullet-}$ provided the indirect measurement of $O_2^{\bullet-}$ concentration. $O_2^{\bullet-}$ was found to be generated by all three shapes of anisotropic AgNPs. Interestingly, there was no statistically significant difference between all three shapes of AgNPs in terms of $O_2^{\bullet-}$ generation.

This discrepancy in superoxide generation between anisotropic AgNPs is most likely due to the atomic structure's difference on NP's surface with their predominant exposed facets. The surface dominated by {100} facets are usually unsaturated with more dangling bonds, which provide the better absorbance of O_2 on its surface, leading to the formation of $O_2^{\bullet-}$.

Similarly, Fig. 8 shows that $^{\bullet}OH$ was detected in all three shapes, with no radical quantitative difference in between each respective shape. In contrast to superoxide generation, the amount of $^{\bullet}OH$ production was considerably lower. The characteristics of NP and their respective quantitative ROS generated by each shape of AgNPs are summarized in Table 2. Moreover, like $O_2^{\bullet-}$, $^{\bullet}OH$ was not detected under dark conditions. No degradation of FFA was noticed, which implied that there was no detectable $^1O_2$. It might be due to the fact that with

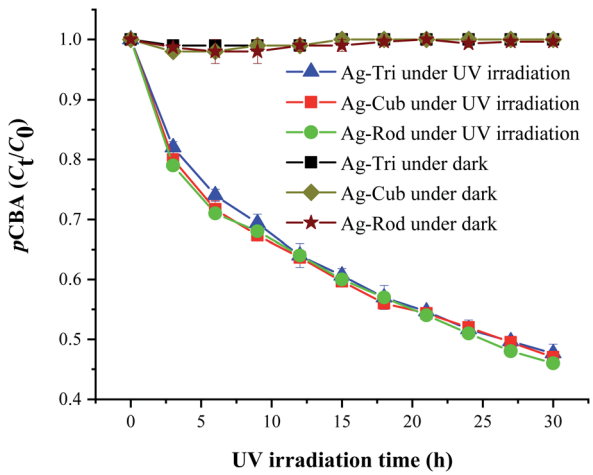

Fig. 8 $^{\bullet}OH$ generation kinetics under UV irradiation of the aqueous suspension of anisotropic AgNPs, as shown by the degradation of 20 μM *p*CBA.

Table 2 Anisotropic silver nanoparticles characteristics and photo-generated ROS quantification data

Nano particle shape	ζ-Potential (mV)	Size range (nm)	Surface modification	$O_2^{\bullet -}$ (μM)	$^{\bullet}OH$ (μM)	$^1O_2$
Ag-Tri	−24.08	28 to 95	UM[a]	69 ± 3.2	11 ± 1.6	ND[b]
Ag-Cub	−20.02	32 to 102	UM[a]	72 ± 2.9	10.4 ± 1.9	ND[b]
Ag-Rod	−19.08	35 to 138	UM[a]	68.5 ± 3.7	11.3 ± 2.2	ND[b]

[a] Unmodified. [b] Not detected.

a very short life span of $^1O_2$, it can get rapidly consumed than that of the other two types of ROS detected in this study. The life span of $^1O_2$ last only 2 μs, whereas that of $^{\bullet}OH$ and $O_2^{\bullet -}$ has a comparatively longer life span of 200 μs and 5 to hundreds of microseconds, respectively. Similar results for $^1O_2$ were reported by Yang and group where they studied the effects of surface-coated dependent ROS generation. In their work, no detectable $1O^2$ was produced.[20] In contrast, Luciana and group reported singlet oxygen generate by silver pectin nanoparticles. They utilized a singlet oxygen sensor green reagent, which is a highly sensitive $1O^2$ detector.[21]

Selective ROS species effect on antimicrobial activity

To study the selective ROS species effect on antimicrobial activity, ROS scavengers (superoxide dismutase (SOD) isopropanol) were used to selectively block $^{\bullet}OH$ and $O_2^{\bullet -}$. The tests were performed on *E. coli* due to comparatively fast action and better performance of anisotropic AgNPs against the tested microbe. The NP concentrations were selected based on MBC values for each nanoparticle shape.

ROS scavengers were added to the NP suspension after UV irradiation. To examine the long-lived $O_2^{\bullet -}$, the NP suspension after addition of isopropanol ($^{\bullet}OH$ scavenger) was kept in the dark for 10 min to ensure the consumption of short-lived ROS ($^{\bullet}OH$ and possibly $^1O_2$). After that, the NP suspension was added to the *E. coli* suspension with an initial bacterial concentration of 10^7 CFU mL^{-1}. Similarly, SOD was added as $O_2^{\bullet -}$ scavenger to examine the antibacterial effect of $^{\bullet}OH$ individually. The antibacterial effect in the absence of the detected ROS ($^{\bullet}OH$ and $O_2^{\bullet -}$) species and reaction under the dark (without UV irradiation) were also conducted to examine the nanoparticles' performance based on their structure alone. The results were expressed in log reduction by using the eqn (3)

$$\text{Log reduction} = \log_{10}\left(\frac{A}{B}\right) \quad (3)$$

where A is the number of viable microbes before treatment and B is the number of organisms after treatment. Log reduction was converted to a percentage reduction for the ease of comparative analysis by using the eqn (4).

$$P = (1 - 10^{-L}) \times 100 \quad (4)$$

Where P is the percent reduction, and L is the log reduction. The effect of Ag ion was subtracted from the final results. Silver ion release was monitored for 5 h. The results showed uniformity in the release of Ag ions by different shapes of AgNPs. Ag ion release remained relatively low (240 μg mL^{-1}), which indicated the structural stability of the as prepared nanoparticles (Fig. 9). However, an evident significant difference was noticed between Ag ion release under UV irradiation and Ag ion release under dark conditions. Upon irradiation, all NP released 5 fold more ions than that of the experiments conducted in the dark.

Fig. 10 shows the selective ROS biocidal performance of anisotropic AgNP. Selective ROS experiments showed Ag-Tri bacterial reduction patterns in Fig. 10(a). The reduction in antibacterial activity was noticed upon the addition of $O_2^{\bullet -}$ scavenger. The antibacterial effect of Ag-Tri dropped down to 60% as compared to neat Ag-Tri (without the addition of any scavengers) by achieving a 40% reduction in the bacterial population in 3 h. With the blockade of $^{\bullet}OH$ scavengers, Ag-Tri continued to perform reasonably high by achieving above 90% bacterial reduction. The maximum reduction in the biocidal property was noticed when both detected ROS species were blocked with their respective scavengers. In the absence of $O_2^{\bullet -}$ and $^{\bullet}OH$, Ag-Tri managed to reduce the *E. coli* population to 20%. Similarly, the little bactericidal effect was noticed for the experiments conducted in the dark.

Fig. 10(b) illustrated that Ag-Cub displayed only 20% cell reduction in 3 h of NP exposure and 30% cell reduction in the absence of $O_2^{\bullet -}$ in 4 h, which showed a 70% drop in antibacterial performance as compared to neat Ag-Cub, while the minimum drop in bactericidal effect was noticed in the absence of $^{\bullet}OH$. Ag-Cub retained above 80% cell reduction without $^{\bullet}OH$.

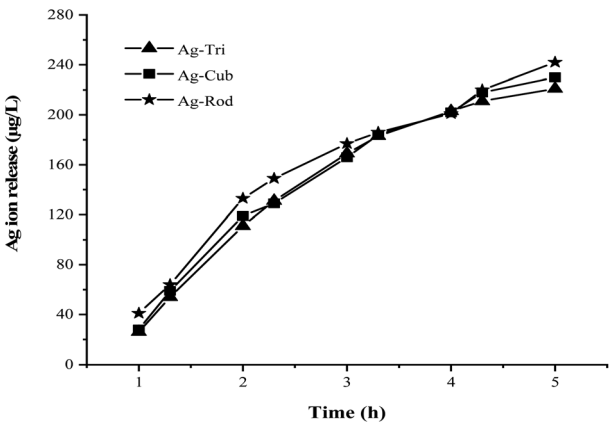

Fig. 9 Silver ion release profile of anisotropic silver nanoparticles with UV irradiation.

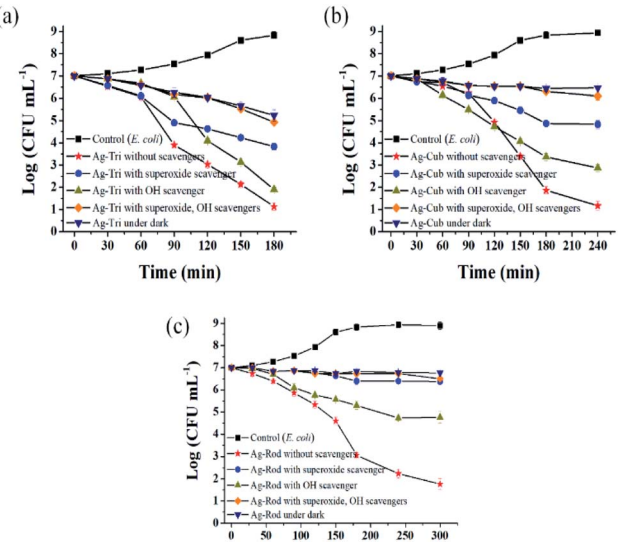

Fig. 10 Anisotropic AgNPs selective ROS specie action on *E. coli*. (a) Ag-Tri selective ROS bactericidal action (b) Ag-Cub ROS action on *E. coli* (c) Ag-Rod individual ROS action with respect to bacterial inactivation.

In the absence of both detected ROS species, Ag-Cub showed a 10% reduction in the *E. coli* population.

Fig. 10(c) shows the selected ROS species results for Ag-Rod were observed with deleterious effect on Ag-Rod's antibacterial performance. Only 5% bactericidal effect was achieved in 5 h of NP exposure when $O_2^{\bullet -}$ was scavenged by SOD. Without the availability of $^{\bullet}OH$ in the NP solution, Ag-Rod managed to achieve around 70% reduction in *E. coli* cells. However, in the absence of both ROS species and the experiments conducted in the dark without UV irradiation, Ag-Rod's antibacterial effect almost ceases to exist. These results showed the consistency with MIC and killing kinetics studies.

These results clearly and consistently demonstrated that among all ROS species, $O_2^{\bullet -}$ is the dominant ROS species, which is primarily responsible for the antibacterial effect of anisotropic AgNPs. Although $O_2^{\bullet -}$ is not considered a strong oxidant, $O_2^{\bullet -}$ in dis-mutation reactions produce $^{\bullet}OH$ and $^1O_2$. The highly reactive and short-lived $^{\bullet}OH$ also played a fair role in displaying a biocidal effect. In this work, $^1O_2$ was not detected, but theoretically, all three ROS may coexist and produce complex oxidative stress on biologically operated systems.[22] Research conducted by Dabin and coworkers illustrated photo-generated ROS related antibacterial activity in TiO_2. They concluded that among all detected ROS species, superoxide was the dominant ROS species responsible for the photo-degradation of rhodamine B.[23] Wen and the group reported photo-generated ROS among various metal nanoparticles and studied their action against *E. coli*. Their results showed that silver nanoparticles exhibited the highest antibacterial effect among gold, nickel and silicon NP, and the dominant ROS species was superoxide radicals.[24]

Ag-Tri continued to display superior biocidal capabilities among all NP used in this study. It is worth noting that in the absence of both ROS species, Ag-Tri was able to reduce double the number of *E. coli* cells than that of Ag-Cub (Ag-Tri 20%, Ag-Cub 10%), which clearly showed the importance of NP morphology and the crystal facet role. It provided direct evidence of the fact that besides ROS action, NP surface morphology played a critical role in determining the overall biocidal effect of anisotropic AgNP. Ag-Tri was dominated by {111} facets, while {100} facets dominated Ag-Cub.

Furthermore, both Ag-Tri and Ag-Rod had the same {111} faceted structures and produced nearly the same amount of photo-generated ROS. However, there was a big difference between the nanoparticles' antibacterial performance, which further confirms the role of nanoparticle morphology, such as sharp tips and direct interaction with bacterial cells. Ag-Rods were found to have rounded-ends morphology and displayed poor contact with bacterial cells (Fig. 6), which might be one reason behind lower Ag-Rod activity.

High antibacterial activity of Ag-Tri can be attributed to the sharp-tip morphology and high-atom-density active {111} facets. The greater reactivity of {111} facets allowed rapid localization on bacterial cell and provided increased interaction with vital proteins present on the bacteria cell's outer surface. Moreover, Triangular silver nanoparticles were found to have the maximum electromagnetic field at their tips compared to other nanoparticle shapes, adding to its reactivity by the rapid facilitation photo-induced redox reaction on these surfaces affecting greatly bacterial cell integrity.[25]

The high performance was attributed to the superior trait of triangular AgNPs such as sharp tip morphology, high-atom-density active {111} facets and high di-electric charge. Densely packed atoms on {111} provide a more significant NP interaction on the bacterial surface.[4] Pal and the group also reported the high performance of triangular AgNPs compared with spherical and rod-shaped AgNPs. They attributed {111} active facets and sharp vertex to be the reason behind the high performance of truncated triangular silver nanoparticles.[3]

4. Conclusion

In this study, three different shapes (triangular, cube and rod) of anisotropic silver nanoparticles were tested against Gram-negative and Gram-positive bacteria for their antibacterial activity. Photo-generated ROS quantification and selective ROS species biocidal capabilities were monitored. All fabricated nanoparticles displayed shape-dependent high antibacterial activity. Besides, the antibacterial performance of anisotropic AgNPs followed the order of Ag-Tri > Ag-Cub > Ag-Rod. Ag-Tri displayed the highest biocidal effect on both bacterial strains. Ag-Tri achieved complete bacterial mutilation in the shortest time of 180 min with the least concentration required to achieve this effect compared to Ag-Cub and Ag-Rod, which required comparatively higher NP concentration and took 240 and 300 min respectively. Furthermore, Photo-generated ROS was almost the same for all NP shapes except Ag-Cub, which showed slightly higher superoxide generation than that of Ag-Tri and Ag-Rod. However, the difference in superoxide generation was not statistically significant. Ag-Rod showed the lowest performance and was unable to achieve 100% bacterial eradication

against both tested bacteria. Moreover, it was revealed that ROS was not the only mechanism responsible for the antibacterial effect. Surface morphology played a vital role in determining the overall biocidal effect of anisotropic AgNPs. Sharp-tip morphologies and high-atom-density active facets were attributed to the high activity of Ag-Tri, which provided more significant direct interaction with bacterial cells. Ag-Tri and Ag-Cub achieved physical bacterial mutilation, but Ag-Rod achieved only bacterial inactivation, and no physical membrane damage was noticed. The work conducted here can serve as a foundation to further investigate the role of surface morphology and to develop structures with controlled facets growth to optimize reactive oxygen species (ROS) production and sensitive detection to evaluate the biocidal effect of myriad shapes of nanoparticles, which are yet to be investigated.

Conflicts of interest

The authors declare no competing financial interest and no conflicts to declare.

Acknowledgements

This work was supported by the National Natural Science Foundation of China Project under grant nos. 51375253, 51703116, and 51775296. The authors also acknowledge the support of this work from the Tsinghua National Laboratory for Information Science and Technology, China, under grant code SKLT2018C06.

Notes and references

1 M. Gao, L. Sun, Z. Wang and Y. Zhao, *Mater. Sci. Eng., C*, 2013, **33**, 397–404.
2 X. Hong, J. Wen, X. Xiong and Y. Hu, *Environ. Sci. Pollut. Res.*, 2016, **23**, 4489–4497.
3 J. Li, L. Yan, H. Li, W. Li, F. Zha and Z. Lei, *J. Mater. Chem. A*, 2015, **3**, 14696–14702.
4 J. Ahmad, X. Wen, F. Li and B. Wang, *RSC Adv.*, 2019, **9**, 6733–6744.
5 J. D. Padmos, R. T. M. Boudreau, D. F. Weaver and P. Zhang, *Langmuir*, 2015, **31**, 3745–3752.
6 N. Dasgupta, S. Ranjan, S. Mundra, C. Ramalingam and A. Kumar, *Int. J. Food Prop.*, 2016, **19**, 700–708.
7 A. G. Memon, X. Zhou, J. Liu, R. Wang, L. Liu, B. Yu, M. He and H. Shi, *J. Hazard. Mater.*, 2017, **321**, 417–423.
8 A. G. Memon, Y. Xing, X. Zhou, R. Wang, L. Liu, S. Zeng, M. He and M. Ma, *J. Hazard. Mater.*, 2019, 120948.
9 J. R. Morones, J. L. Elechiguerra, A. Camacho, K. Holt, J. B. Kouri, J. T. Ramírez and M. J. Yacaman, *Nanotechnology*, 2005, **16**, 2346–2353.
10 S. Agarwal, L. Lefferts, B. L. Mojet, D. A. J. M. Ligthart, E. J. M. Hensen, D. R. G. Mitchell, W. J. Erasmus, B. G. Anderson, E. J. Olivier, J. H. Neethling and A. K. Datye, *ChemSusChem*, 2013, **6**, 1898–1906.
11 C.-Y. Chiu, P.-J. Chung, K.-U. Lao, C.-W. Liao and M. H. Huang, *J. Phys. Chem. C*, 2012, **116**, 23757–23763.
12 C.-L. Lee, Y.-L. Tsai, C.-H. Huang and K.-L. Huang, *Electrochem. Commun.*, 2013, **29**, 37–40.
13 W. Freinbichler, M. A. Colivicchi, C. Stefanini, L. Bianchi, C. Ballini, B. Misini, P. Weinberger, W. Linert, D. Varešlija, K. F. Tipton and L. Della Corte, *Cell. Mol. Life Sci.*, 2011, **68**, 2067–2079.
14 H. H. Lara, E. N. Garza-Treviño, L. Ixtepan-Turrent and D. K. Singh, *J. Nanobiotechnol.*, 2011, **9**, 30.
15 D. Acharya, K. M. Singha, P. Pandey, B. Mohanta, J. Rajkumari and L. P. Singha, *Sci. Rep.*, 2018, **8**, 201.
16 R. Sonohara, N. Muramatsu, H. Ohshima and T. Kondo, *Biophys. Chem.*, 1995, **55**, 273–277.
17 Q. L. Feng, J. Wu, G. Q. Chen, F. Z. Cui, T. N. Kim and J. O. Kim, *J. Biomed. Mater. Res.*, 2000, **52**, 662–668.
18 S.-K. Kim, J.-K. Im, Y.-M. Kang, S.-Y. Jung, Y. L. Kho and K.-D. Zoh, *J. Hazard. Mater.*, 2012, **201–202**, 82–91.
19 I. P. Mukha, A. M. Eremenko, N. P. Smirnova, A. I. Mikhienkova, G. I. Korchak, V. F. Gorchev and A. Y. Chunikhin, *Appl. Biochem. Microbiol.*, 2013, **49**, 199–206.
20 Y. Li, W. Zhang, J. Niu and Y. Chen, *Environ. Sci. Technol.*, 2013, **47**, 10293–10301.
21 L. S. A. de Melo, A. S. L. Gomes, S. Saska, K. Nigoghossian, Y. Messaddeq, S. J. L. Ribeiro and R. E. de Araujo, *J. Fluoresc.*, 2012, **22**, 1633–1638.
22 I. Fridovich, *Arch. Biochem. Biophys.*, 1986, **247**, 1–11.
23 D. Wang, L. Zhao, L.-H. Guo and H. Zhang, *Anal. Chem.*, 2014, **86**, 10535–10539.
24 W. Zhang, Y. Li, J. Niu and Y. Chen, *Langmuir*, 2013, **29**, 4647–4651.
25 I. Pastoriza-Santos and L. M. Liz-Marzán, *J. Mater. Chem.*, 2008, **18**, 1724–1737.